Engineering 3 (2017) 708–715

Contents lists available at ScienceDirect

Engineering

journal homepage: www.elsevier.com/locate/eng

Research
Additive Manufacturing—Article

A Large Range Flexure-Based Servo System Supporting Precision Additive Manufacturing

Zhen Zhang [a,b,c], Peng Yan [d,*], Guangbo Hao [e,*]

[a] State Key Laboratory of Tribology & Institute of Manufacturing Engineering, Tsinghua University, Beijing 100084, China
[b] Beijing Key Laboratory of Precision/Ultra-Precision Manufacturing Equipment and Control, Tsinghua University, Beijing 100084, China
[c] Department of Mechanical Engineering, Tsinghua University, Beijing 100084, China
[d] Key Laboratory of High-Efficiency and Clean Mechanical Manufacturing, Ministry of Education, School of Mechanical Engineering, Shandong University, Jinan 250061, China
[e] Department of Electrical and Electronic Engineering, University College Cork, Cork, Ireland

ARTICLE INFO

Article history:
Received 7 September 2017
Revised 24 September 2017
Accepted 25 September 2017
Available online 25 October 2017

Keywords:
Precision additive manufacturing
Micro-stereolithography
Nanopositioning
Beam flexure

ABSTRACT

This paper presents the design, development, and control of a large range beam flexure-based nano servo system for the micro-stereolithography (MSL) process. As a key enabler of high accuracy in this process, a compact desktop-size beam flexure-based nanopositioner was designed with millimeter range and nanometric motion quality. This beam flexure-based motion system is highly suitable for harsh operation conditions, as no assembly or maintenance is required during the operation. From a mechanism design viewpoint, a mirror-symmetric arrangement and appropriate redundant constraints are crucial to reduce undesired parasitic motion. Detailed finite element analysis (FEA) was conducted and showed satisfactory mechanical features. With the identified dynamic models of the nanopositioner, real-time control strategies were designed and implemented into the monolithically fabricated prototype system, demonstrating the enhanced tracking capability of the MSL process. The servo system has both a millimeter operating range and a root mean square (RMS) tracking error of about 80 nm for a circular trajectory.

1. Introduction

Micro-additive manufacturing (micro-AM) is considered to be an effective method to improve the performance of three-dimensional (3D) microproducts. Scalable AM is classified as one of the main groups of micro-AM, and includes stereolithography (SL), selective laser sintering (SLS), and inkjet printing; these technologies can be employed at both the macroscale and microscale in order to efficiently fabricate complex 3D components.

As one of the most popular scalable AM technologies, SL solidifies a liquid polymer by photo-curing with high resolution. Micro-stereolithography (MSL) [1–3] is SL at the microscale, and is widely used in many areas, such as microsensors [4], optical waveguides [5], 3D photonic band gap structures [6], and biology analysis [7]. During an MSL process, a two-dimensional (2D) microscale pattern is formed by solidifying a liquid photopolymer; next, a 3D structure can be obtained by accumulating the 2D patterns. An MSL system is mainly composed of a liquid resin container and a precision multi-axis motion stage, with which the patterns are accurately located with the laser beam in order to solidify the resin.

The accuracy of the finished product is determined by both the solidified area generated by the light beam and the motion quality of the positioning system. In other words, the motion system must be accurate and repeatable enough to reach the right location for every solidification event. A considerable amount of research effort has been devoted to reducing the laser spot size; examples include Refs. [8–10] and the references therein. However, relatively fewer works emphasize the motion quality of positioning systems, possibly

* Corresponding authors.
E-mail addresses: pengyan2007@gmail.com; g.hao@ucc.ie

http://dx.doi.org/10.1016/J.ENG.2017.05.020

because the required motion quality corresponding to the laser spot size is not particularly stringent. Given the recent decrease of the laser spot size down to 1 μm or less [10], the corresponding motion quality should be one order of magnitude less than the laser spot size—that is, < 100 nm. This means that a nano precision stage is required in order to achieve nanometric motion quality. In order to achieve such a high-precision motion quality, the choice of the bearings of the motion stages is crucial. Most current multi-axis positioning stages are based on contact bearings, such as linear guideways, which limit the motion quality to the sub-micrometer level; moreover, this type of design requires sophisticated assembly and maintenance.

With the goal of providing a nanopositioning system to support MSL systems, this paper discusses the development of a beam flexure-based motion system. To overcome the abovementioned disadvantages of contact bearings, it is desirable to have a motion system that uses frictionless bearings. Flexure bearings provide motion by means of the elastic deformation of flexures, which allows nondeterministic effects such as friction, backlash, and wear to be avoided during the operation; as a result, nanometric motion quality can be achieved in a compact desktop size. Furthermore, beam flexure-based nanopositioning systems are extremely suitable for harsh operation environments, as zero maintenance is required. By combining multiple beam flexures, a flexure mechanism can be constructed to provide millimeter-range (or even centimeter-range) motion guidance and load bearing in a compact desktop size [11,12]. Despite the abovementioned advantages of flexure bearings, some challenges still exist in the design and control of beam flexure-based nanopositioning systems. In research into the development of over-millimeter-range *XY* micropositioners (e.g., Refs. [12,13]), the actual motion quality of these systems were not fully satisfactory, with very few experimental results showing nanometric tracking accuracy (< 100 nm). As one of the aims of this work, we would like to emphasize mechanism design and real-time control strategies in order to show the nanometric tracking accuracy of large range beam flexure-based nanopositioner supporting MSL systems.

The remainder of this paper is organized as follows: In Section 2, the design of a large range beam flexure-based nanopositioning stage is discussed, with detailed finite element analysis (FEA) and verification. In Section 3, a real-time control system is proposed for trajectory tracking of the nanopositioning system, and in Section 4, numerous experiments are conducted on the fabricated prototype system to demonstrate the desired ability of the nano servo system.

2. A beam flexure-based nanopositioning stage supporting MSL systems

A schematic design of a beam flexure-based MSL system is shown in Fig. 1. The main components of the MSL system and their features are briefly introduced. A light source and a related optical system are responsible for generating a small laser beam (with a spot size of < 1 μm) to induce photo-curing. For the sake of compact size, a Blu-ray optical pickup unit (OPU) can be chosen as the light source [14]. The multi-axis motion system is mainly composed of two positioning stages. One is an *XY* nanopositioning stage; this is the key to precisely locating the laser beam in an *XY* plane, such that the *XY* cross-sections of a 3D micro component can be solidified. When the laser spot size goes down to 1 μm or less, a nanometric motion quality of the *XY* motion stage is required. The development of such a nanopositioning system in a compact desktop size is challenging and is the main concern of this work. The other positioning stage is a *Z*-axis translator, which is responsible for providing the required vertical motion of one layer thickness of the sliced 3D component. Since the motion quality of the *Z*-axis translator is at the micrometer level, this solution is widely available and hence is not under consideration in this study.

With the abovementioned motion requirement in mind, we present a compact beam flexure-based nanopositioning stage supporting MSL system. To be specific, an *XY* nanopositioning stage was designed to locate the laser beam in a range of 3 mm along both *X* and *Y* axes. For this range, electromagnetic actuators such as voice coil actuators (VCAs) are usually adopted to provide thrust forces.

Instead of obvious but bulky serial kinematic configuration of the *XY* positioning stage, in which one axis stacks on top of another, we considered a parallel kinematic configuration of the flexure mechanism, in which each axis actuator is grounded mounted. With this type of configuration, a higher bandwidth and precision of the motion system can be achieved due to the lack of moving actuators and disturbance from moving cables, respectively. Furthermore, in order to achieve a millimeter range and nanometric motion quality of the *XY* parallel mechanism, it is necessary to carefully manage parasitic error motions, which are the motions in any axis that differ from the axis of an applied thrust force. With the increase of the stroke, the in-plane parasitic error motion of the moving stage also increases, including parasitic translational and rotational motions, both of which significantly adversely affect the nanometric motion quality. To reduce the parasitic motions, a mirror-symmetric arrangement is desired, and appropriate planar redundant constraints are usually required in order to reject various disturbances.

Fig. 2 shows a conceptual design, in which the Z-shaped and Π-shaped parallelogram beam flexures provide the required load bearing and kinematic decoupling, and the four-beam flexure serves as the redundant constraints to improve the disturbance-rejection capability of the mechanism. As shown in later sections, the important

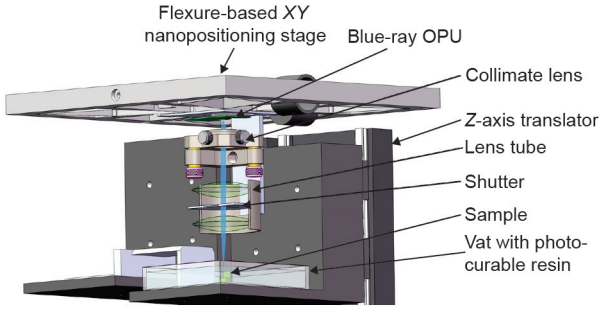

Fig. 1. Schematic design of a beam flexure-based MSL system.

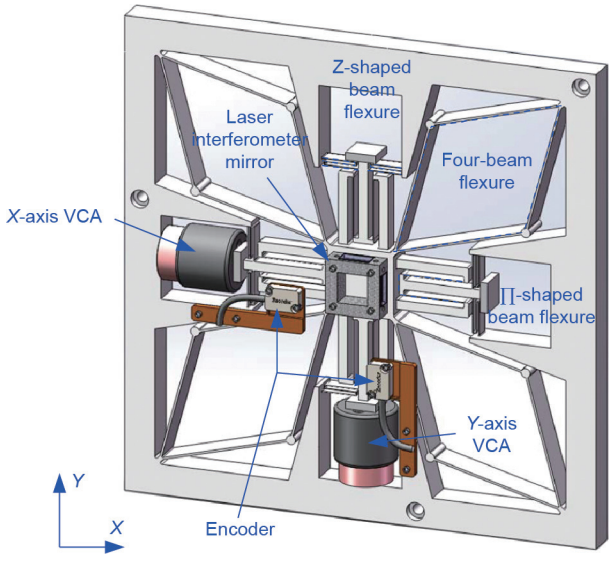

Fig. 2. A large range beam flexure-based *XY* nanopositioner.

features of the design are as follows: A mirror-symmetric arrangement is clearly beneficial to reduce parasitic motion; the transverse stiffness of the Z-shaped beam flexure has a good linear behavior in the desired operation range, which is beneficial toward achieving a large workspace; and the planar redundant constraints provide a sufficiently high stiffness, resulting in significantly reduced parasitic error motions.

Note that there is a tradeoff in the Z-shaped beam flexure design between the desirable and non-desirable characteristics. Regarding desirable characteristics, the Z-shaped beam flexure has a large range of motion, with constant primary stiffness and a very compact structure. Regarding non-desirable characteristics, the Z-shaped beam flexure, as the guiding bearing of the actuator, can also result in non-negligible parasitic transverse motion to the actuator, since it is not a rigorous single-degree-of-freedom compliant prismatic joint. However, this small parasitic motion can be compensated for by the VCA used in this paper.

2.1. Modeling and analysis

Functionally speaking, the motion stage can still achieve a planar motion without redundant constraints; however, an appropriate redundant constraints module is crucial in order to allow the motion stage to achieve a nanometric quality. Several recent studies have reported on the design of redundant constraints to restrict parasitic error motions; examples include Refs. [15–17].

Stiffness model

To establish the functional relationship between the force and dimensions, the stiffness of the proposed mechanism is modeled as follows. The equivalent transverse stiffness k of the overall beam flexure-based mechanism consists of Z-shaped modules $k_{Z,t}$, parallelogram modules $k_{\Pi,t}$, and redundant constraints (four-beam) modules $k_{4\text{beam}}$. The overall stiffness model is shown in Fig. 3, and the equivalent transverse stiffness k of each axis is determined as follows:

$$k = 2k_{Z,t} + 2k_{\Pi,t} + k_{4\text{beam}} \tag{1}$$

Fig. 4 shows the detailed geometry of Z-shaped and Π-shaped beam flexures, where the geometric parameters can be read directly. In Fig. 3, the subscript i denotes the ith module, and $\bar{k}$ denotes the rotational stiffness; for example, $\bar{k}_{Z,i}$ is the rotational stiffness of the ith Z-shaped module. Other geometric parameters can be read directly.

A detailed derivation of each part of the equivalent stiffness (Eq. (1)) is provided in Ref. [18], and the results of each part are described below. The transverse stiffness of two Z-shaped beam flexures is determined as follows:

$$k_{Z,t} = \frac{8EI}{h^3} \tag{2}$$

where h, I, and E are the length of each side of the Z-shaped beam flexure, the moment of inertia, and the Young's modulus, respectively. It is worth noting that the transverse stiffness is linear, which is advantageous in the conventional parallelogram case, in which the transverse stiffness is nonlinear and heavily dependent on the deflection in the transverse direction. Verification of the stiffness model shown above is provided in Subsection 2.3.1. The transverse stiffness of the Π-shaped module has the following closed form [19]:

$$k_{\Pi,t} \approx \frac{24EI + 1.2P_{\Pi}h_6^2}{h_6^3} \tag{3}$$

where h_6 is the length of the Π-shaped beam flexure, and P_{Π} is the axial force of the Π-shaped beam flexure. Note that the transverse stiffness depends on the applied force. It is difficult to obtain a closed form of the stiffness of the four-beam flexure, $k_{4\text{beam}}$, in each axis; however, the stiffness can be obtained numerically by solving a set of algebraic equations governed by geometric deformation and the composite force in each axis. A detailed derivation is provided in Ref. [18].

2.2. Dynamic model

To control the abovementioned nanopositioning stage, the dynamics of each axis are needed. From a dynamics perspective, the VCAs and beam flexure-based mechanism can be treated as a mass-spring system. Furthermore, by using the stiffness model provided above and by neglecting the beam mass, the dynamics can be modeled as a five-mass-spring system (Fig. 3), in which the dynamics of the moving stage m along the X axis, Y axis, and rotational axis are

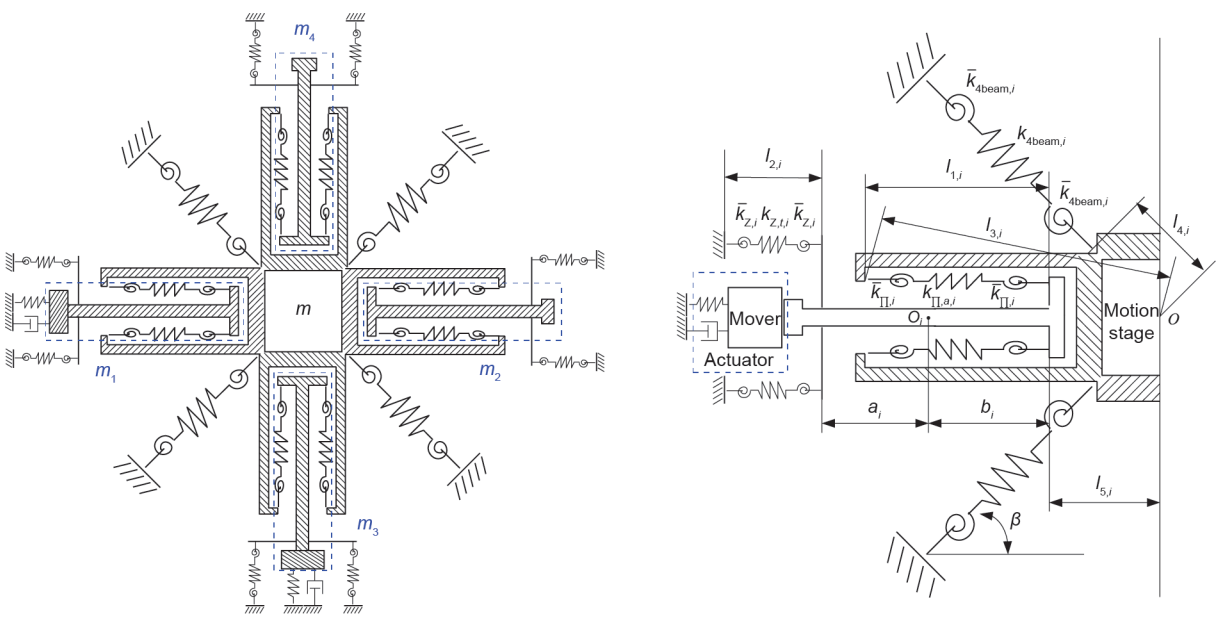

Fig. 3. Overall stiffness model of the *XY* nanopositioning stage.

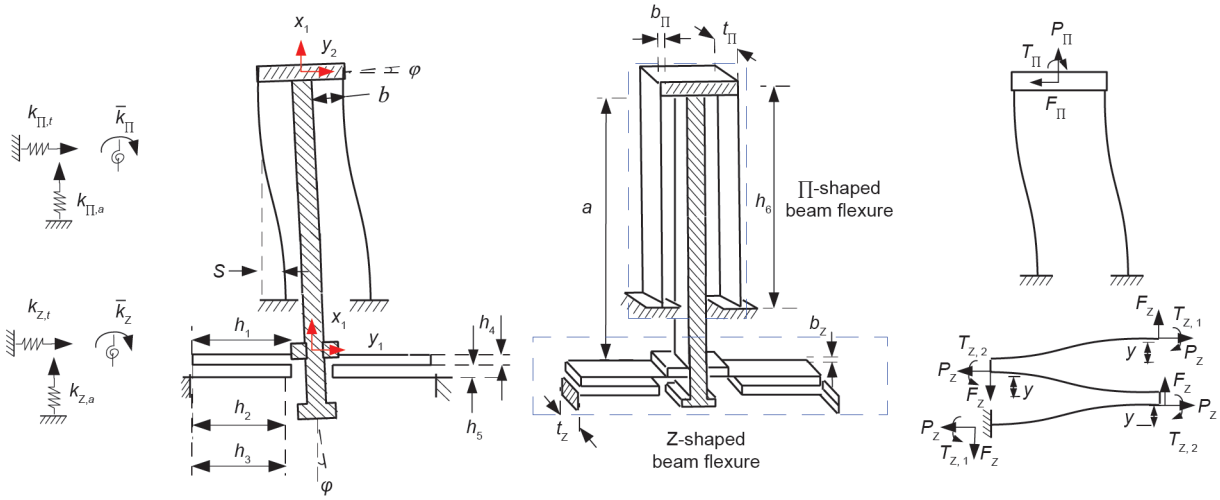

Fig. 4. The geometry of the Z-shaped and Π-shaped beam flexures and their equivalent stiffness model.

modeled as follows:

$$\begin{cases} m\ddot{X}+2\sum_{i=1}^{2}k_{\Pi,a,i}(X-x_i)-2\sum_{i=3}^{4}\frac{\bar{k}_{\Pi,i}}{l_{1,i}}x_i+\sum_{i=1}^{4}\frac{\bar{k}_{4\text{beam},i}}{l_{4,i}}X+\sum_{i=1}^{4}k_{4\text{beam},i}X\cos\beta=0 \\ m\ddot{Y}+2\sum_{i=3}^{4}k_{\Pi,a,i}(Y-y_i)-2\sum_{i=1}^{2}\frac{\bar{k}_{\Pi,i}}{l_{1,i}}y_i+\sum_{i=1}^{4}\frac{\bar{k}_{4\text{beam},i}}{l_{4,i}}Y+\sum_{i=1}^{4}k_{4\text{beam},i}Y\cos\beta=0 \\ I\ddot{\Theta}+2\sum_{i=1}^{4}\frac{\bar{k}_{\Pi,i}l_{3,i}^2}{l_{1,i}}\Theta+\sum_{i=1}^{4}\bar{k}_{4\text{beam},i}l_{i,4}\Theta+2\sum_{i=1}^{2}\bar{k}_{\Pi,i}l_{5,i}x_i+2\sum_{i=3}^{4}\bar{k}_{\Pi,i}l_{5,i}y_i=0 \end{cases} \quad (4)$$

The dynamics of m_1 to m_4 can be derived in a similar way. With the dynamic equations of the five sets of mass, the dynamics from the thrust force to the displacement along the X axis are written in the following compact form:

$$\begin{pmatrix}\dot{X}\\ \ddot{X}\end{pmatrix}=\begin{pmatrix}0 & I\\ -M^{-1}K & 0\end{pmatrix}\begin{pmatrix}X\\ \dot{X}\end{pmatrix}+\begin{pmatrix}0\\ M^{-1}\end{pmatrix}F_X \quad (5)$$

where $M := \text{diag}(m, m_1, m_2, m_3, m_4)$ is the mass matrix, K is the stiffness matrix, and F_X is the thrust force applied to the X axis. The set of design parameters is given in Table 1, and the dimensions of the stage are 330 mm × 330 mm.

By solving Eq. (3), the natural frequency ω of the designed nanopositioning system can be obtained. Substitution of the geometry parameters in stiffness matrix K yields 59.8 Hz as the natural frequency in the X axis and Y axis.

$$\begin{vmatrix} K_{11}-\omega^2 m & -2\frac{\bar{k}_{\Pi,3}}{l_{1,3}} & -2\frac{\bar{k}_{\Pi,4}}{l_{1,4}} \\ -2\frac{\bar{k}_{\Pi,3}}{l_{1,3}} & 2\left(\frac{\bar{k}_{Z,3}}{l_{2,3}}+\frac{\bar{k}_{\Pi,3}}{l_{1,3}}\right)-\omega^2 m_3 & 0 \\ -2\frac{\bar{k}_{\Pi,4}}{l_{1,4}} & 0 & 2\left(\frac{\bar{k}_{Z,4}}{l_{2,4}}+\frac{\bar{k}_{\Pi,4}}{l_{1,4}}\right)-\omega^2 m_4 \end{vmatrix}=0 \quad (6)$$

where $K_{11}=\sum_{i=1}^{4}\left(\frac{\bar{k}_{4\text{beam},i}}{l_{4,i}}+k_{4\text{beam},i}\cos\beta\right)$.

2.3. Finite element analysis

2.3.1. Stiffness model validation

An FEA analysis was conducted to simulate the relationship between the displacement and thrust force. To be specific, in order to achieve higher accuracy of the solution, a high mesh density and a large deflection approach were utilized for the Z-shaped module, the parallelogram module, and the redundant constraints module. The material of the stage was aluminium alloy 7075-T6, which has the following properties: Young's modulus, 72 GPa; Poisson's ratio, 0.3; and density, 2.7×10^{-6} kg·mm^{-3}. The FEA result shows that the maximum ranges of the X and Y axes are 1.5003 mm, which agrees with the analytical ranges. In addition, it is seen from Fig. 5 that the transverse stiffness change is about 0.276% when the force varies from 10 N to 60 N, which validates the linear stiffness model in Eq. (2).

2.3.2. Modal analysis

Modal analysis results by ANSYS are shown in Fig. 6, where the redundant constraints (four-beam) modules mainly correspond to the first two modals (Fig. 6(a-i) and (a-ii)). In addition, the rotation corresponds to the third modal (Fig. 6(a-iii)), and the vibration of

Table 1
The optimized parameters of the proposed nanopositioner.

Parameter	Geometric size (mm)
The length of Π-shaped beam flexure, l_Π	40.0
The height of Π-shaped beam flexure, d_Π	10.0
The width of Π-shaped beam flexure, t_Π	0.4
The length of four-beam flexure, $l_{4\text{beam}}$	80.0
The width of four-beam flexure, $t_{4\text{beam}}$	1.3
The width of Z-shaped beam flexure, t_Z	0.4

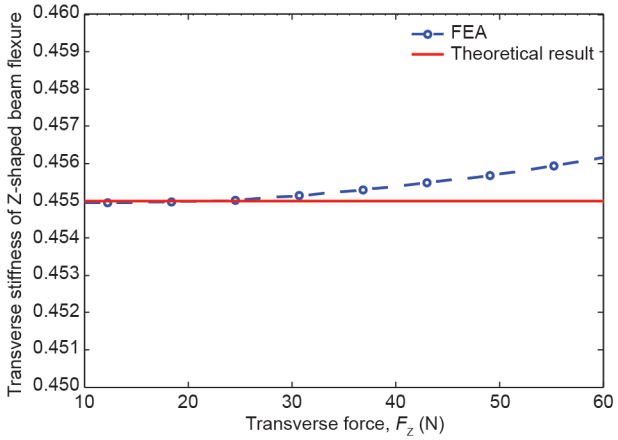

Fig. 5. FEA result of the normalized stiffness of the Z-shaped beam flexure.

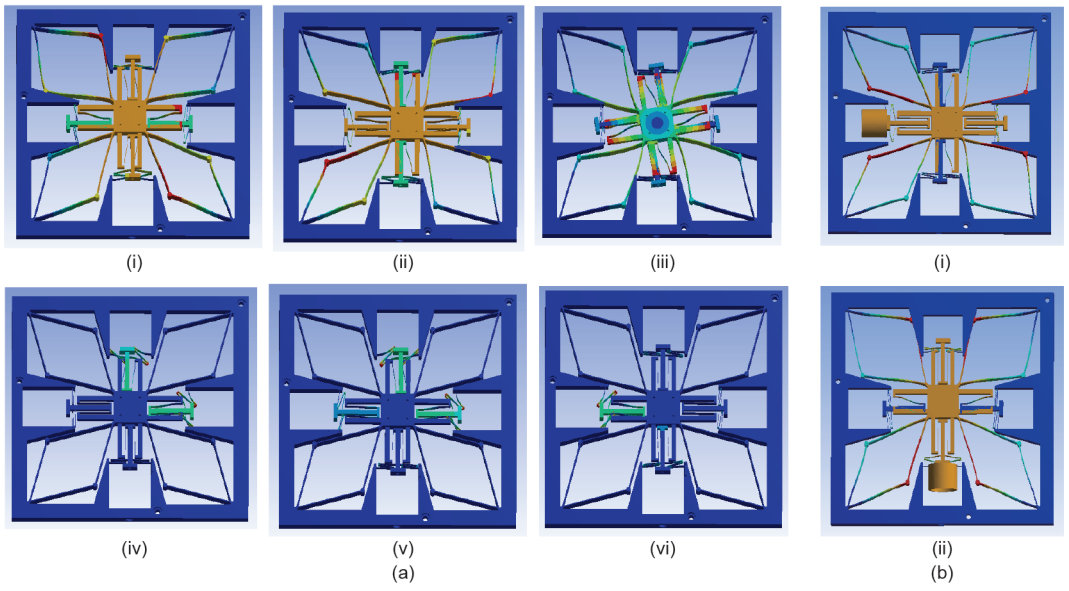

Fig. 6. FEA results of modal analysis. (a) FEA result of the first six order modals: (i) 1st modal (76.1 Hz); (ii) 2nd modal (76.3 Hz); (iii) 3rd modal (126.3 Hz); (iv) 4th modal (243.1 Hz); (v) 5th modal (243.6 Hz); (vi) 6th modal (245.2 Hz). (b) FEA result of the *X* and *Y* axes: (i) modal of *X* axis (55.0 Hz); (ii) modal of *Y* axis (55.4 Hz).

the T-shaped connecting component corresponds to the fourth to sixth modals (Fig. 6(a-iv)–(a-vi)), which are far beyond the working frequency range.

2.3.3. Validation of the redundant constraints module

To better illustrate the advantages of the proposed design, we compared the performance of the proposed design with that of the same design in the absence of the (four-beam) redundant constraints module. The following two sets of comparisons were conducted: First, a 1 mm displacement was applied to the primary motion axis; simultaneously, a 0.01 mm off-axis displacement was applied, which was perpendicular to the primary motion axis in order to simulate disturbances. The resulting error motions of the moving stage reflected the disturbance-rejection capability of the proposed design. Next, modal analysis was conducted to show the difference in the natural frequencies of the two cases. The results are shown in Table 2: The error motion is 87.1 nm versus 193.8 nm, and the natural frequency is 55.0 Hz versus 44.1 Hz. It is clear that the proposed design has a much better disturbance-rejection capability and a higher bandwidth.

Table 2
FEA comparison between the proposed design and the same design without a four-beam redundant constraint.

	Error motion	Natural frequency
Without four-beam redundant constraint	193.8 nm	44.1 Hz
With four-beam redundant constraint	87.1 nm	55.0 Hz
Improvement	55.1%	24.7%

3. Real-time control system

To precisely control the motion system in an accurate and repeatable fashion, a real-time control system is required, for which advanced feedback control strategies need to be appropriately designed. The overall control system we propose here has the following features:

- Enhanced tracking performance for high-frequency signals with minimized tracking errors; and
- Powerful, user-friendly controllers and drives to enhance the positioning process.

For enhanced dynamic performance for different circumstances, numerous control algorithms, such as robust control, repetitive control, disturbance observer, notch filer, and so forth, are combined within the control architecture. Due to space limitations, we will highlight the controller design to optimize the robustness during performance and prevent uncertainties. In particular, we denote $S(s)$ and $T(s)$, which are the sensitivity and complementary sensitivity of the plant model $G(s)$, respectively, as follows:

$$S(s)=\frac{1}{1+G(s)C(s)} \tag{7}$$

$$T(s)=\frac{G(s)C(s)}{1+G(s)C(s)} \tag{8}$$

where $C(s)$ is a feedback controller to be designed. The controller synthesis can now be formulated by means of a mixed sensitivity H_∞ optimization, as follows:

$$C_{\text{opt}}(s):=\inf_{C_{\text{stab}},G}\left\|\begin{bmatrix}W_1(s)S(s)\\W_2(s)T(s)\end{bmatrix}\right\|_\infty \tag{9}$$

The optimal H_∞ index γ_{opt} can be explicitly expressed as follows:

$$\gamma_{\text{opt}}=\left\|\begin{bmatrix}W_1(s)\left[1+G(s)C_{\text{opt}}(s)\right]^{-1}\\W_2(s)\left[G(s)C_{\text{opt}}(s)\right]\left[1+G(s)C_{\text{opt}}(s)\right]^{-1}\end{bmatrix}\right\|_\infty \tag{10}$$

where $W_1(s)$ and $W_2(s)$ are the performance weighting and uncertainty weighting functions, respectively.

To accommodate controller algorithms for real-time implementation, a user-friendly interface was also developed with the following features:

- Output zeroing, linearization, and temperature compensation;
- Sensor calibration and temperature compensation;
- High sampling frequency feedback control of the firmware architecture;
- Complex trajectory tracking; and
- User program space and data space through the callback functions.

4. Experimental results

4.1. Experimental setup

Fig. 7 shows the prototype of the large range *XY* beam flexure-based nanopositioner. The prototype was monolithically fabricated from aluminium alloy 7075-T6 via wire electric discharge machining. Two VCAs were utilized to actuate the servo stage. A Renishaw laser interferometer was used to sense and feedback the displacements of the motion stage for a large range of up to 1.5 mm × 1.5 mm. A feedback control strategy was employed by a self-designed rapid-prototyping control system (Fig. 8), which is an open architecture. Fig. 9 shows the user interface running on the host computer.

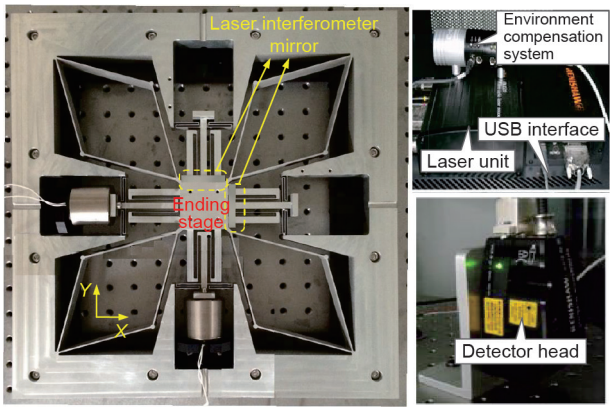

Fig. 7. Prototype of the large range *XY* beam flexure-based nanopositioner.

Due to the symmetrical configuration, the system has an identical model on both actuation axes. The overall dynamics of the motion system are composed of electrical and mechanical subsystems. Since the current amplifier was designed with a bandwidth of 2 kHz, it can be assumed that the dynamics from the controlled voltage input to the amplified current are a constant gain.

4.2. Control performance

4.2.1. Stroke analysis

We tested the stiffness of the motion system from the VCA input voltages to the axial displacement. Fig. 10 shows that the nano servo system has a good linear stiffness in the range [0, 1.5 mm]. The *Y* axis was also tested and yielded a similar result, showing that the nano-positioning system has the ability to achieve a ±1.5 mm × 1.5 mm motion range.

4.2.2. Spectrum analysis

To test the frequency response functions (FRFs) of the designed beam flexure-based nanopositioning stage, an impact excitation was

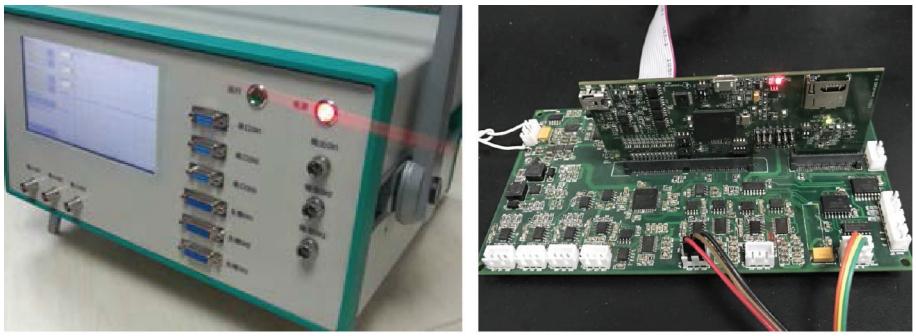

(a) (b)

Fig. 8. Real-time control system. (a) Control box; (b) real-time control board.

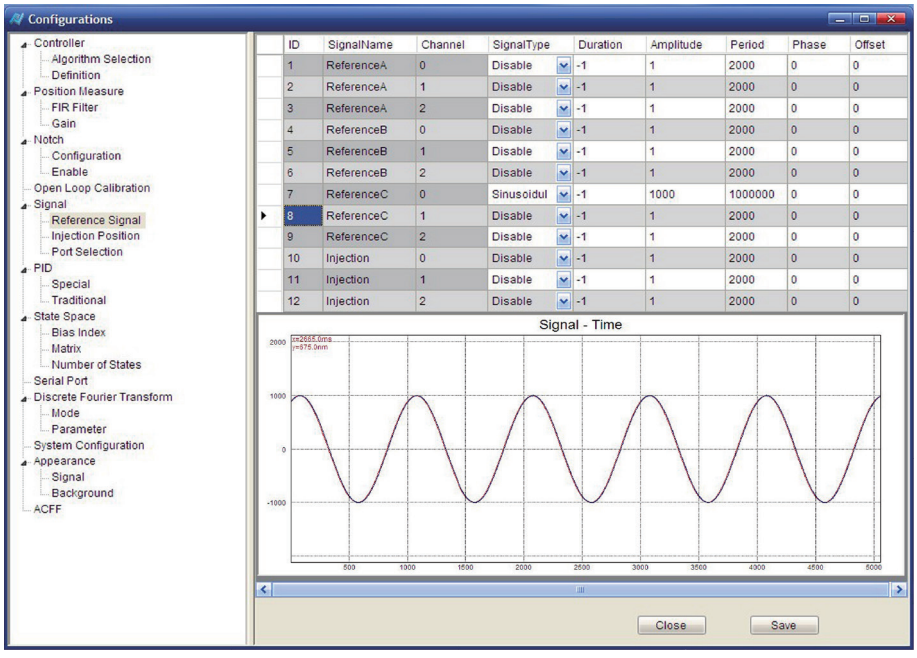

Fig. 9. Host computer interface.

exerted on the system using an impact hammer. The vibration of the servo stage was detected, and the measured signals were processed and then imported to a computer using Fourier analysis to obtain the FRFs of the designed system. The results for the *X* axis are shown in Fig. 11, and the results for the *Y* axis are similar and hence omitted. An obvious resonant peak was observed at 244.2 Hz. Theoretical and FEA results are in very good agreement for the fourth to the sixth orders, at 243.1 Hz, 243.6 Hz, and 245.2 Hz (Fig. 6); in addition, the first and second orders, at 76.1 Hz and 76.3 Hz, can be seen with a resonant peak of 71.2 Hz.

4.2.3. Motion control

To realize precision control for the nano servo system, its dynamics model was needed in advance. The frequency response of each axis was identified, and the identified models for the *X* and *Y* axes were obtained in the following transfer functions, respectively:

$$G_X(s)=\frac{54.2}{s^2+13.6s+103\ 383.8} \tag{11}$$

and

$$G_Y(s)=\frac{51.3}{s^2+17.3s+128\ 584.9} \tag{12}$$

for which the natural frequencies are 51.2 Hz and 57.1 Hz, respectively. These results agree with the FEA results of 55.0 Hz and 55.2 Hz.

To show the contour-tracking performance of the nano servo system, an H_∞ controller, as discussed in Section 3, was designed for the motion stage. The desired trajectory of each axis was set to be a sinusoidal signal of amplitude 0.5 mm and frequency 5 Hz, but with a phase difference of 0.5π rad. The resulting weighting functions were obtained as follows:

$$W_1(s)=\frac{51}{s^2+0.02s+0.0001} \tag{13}$$

$$W_2(s)=\frac{15.99s^2+1.306\times10^4 s+2.667\times10^6}{16.68s^2+1.886\times10^4 s+5.334\times10^6} \tag{14}$$

Based on the above H_∞ optimization, a robust stabilizer of six orders was obtained; its detailed expression is omitted here. The contour-tracking capability is shown in Fig. 12; the root mean square (RMS) error of the circular trajectory is 79.3 nm. In addition, the repeatability of the contour-tracking performance was tested through multiple trials, and the RMS mean tracking error was found to be 84.1 nm.

5. Conclusions

In this work, a large range beam flexure-based nanopositioning system was developed to support the MSL process. This paper provided the design, modeling, FEA analysis, and real-time control system for the nano servo system. Its static and dynamic models are presented here in order to predict the desired system performance. Detailed FEA results showed good agreement between theoretical and simulated calculations. Using the fabricated nano servo stage

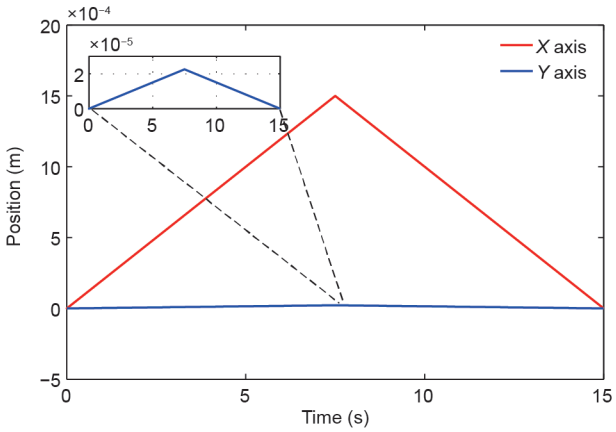

Fig. 10. The experimental result of the parasitic motion.

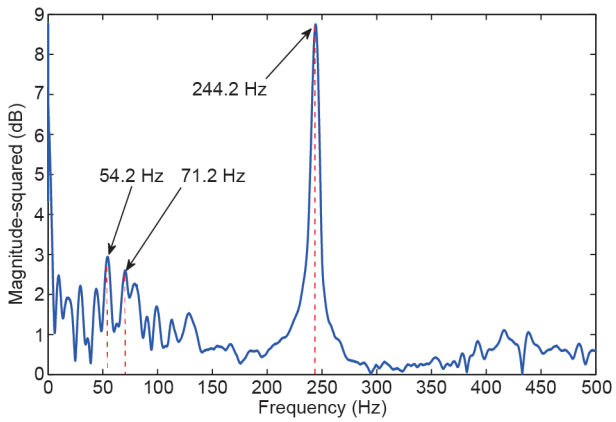

Fig. 11. Modal analysis of the beam flexure-based stage: Resonant frequency without actuators.

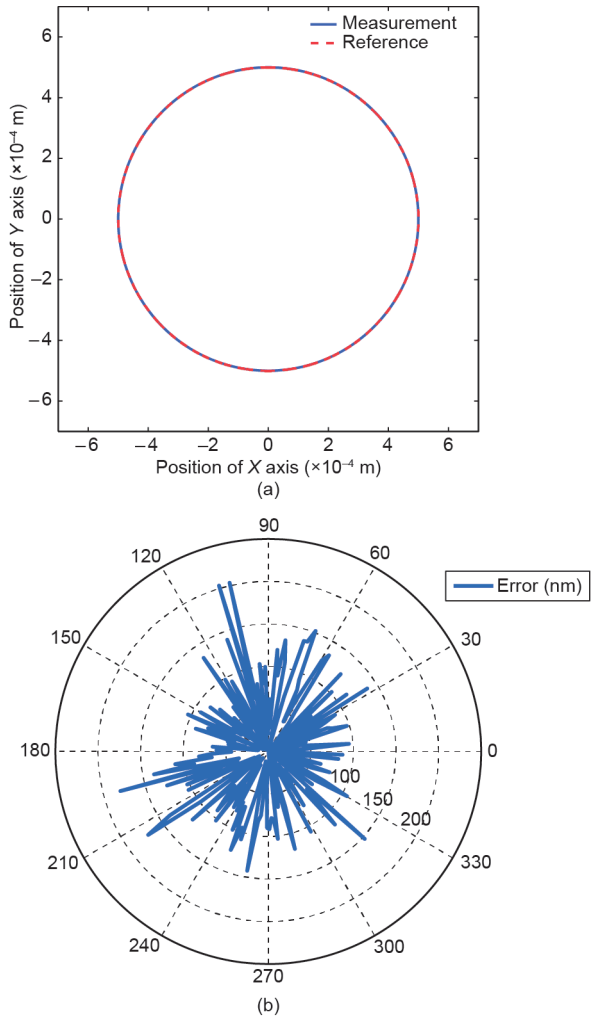

Fig. 12. Experimental result of bi-axis contour tracking. (a) Circular tracking result; (b) tracking error in the polar coordinates.

and its identified dynamic models, real-time advanced control strategies were designed and deployed, showing this system's capability to achieve a millimeter workspace and an RMS tracking error of about 80 m for a circular trajectory.

Acknowledgements

The authors would like to acknowledge support from the Open Foundation of the State Key Laboratory of Tribology & Institute of Manufacturing Engineering (SKL2016B05), and the National Natural Science Foundation of China (NSFC) (61327003).

Compliance with ethics guidelines

Zhen Zhang, Peng Yan, and Guangbo Hao declare that they have no conflict of interest or financial conflicts to disclose.

References

[1] Ikuta K, Hirowatari K. Real three dimensional micro fabrication using stereo lithography and metal molding. In: Proceedings of the IEEE International Workshop on Micro Electro Mechanical Systems: An Investigation of Micro Structures, Sensors, Actuators, Machines and Systems; 1993 Feb 7–10; Fort Lauderdale, FL, USA. Piscataway: The Institute of Electrical and Electronics Engineers, Inc.; 1993. p. 42–7.
[2] Ikuta K, Maruo S, Kojoma S. New micro stereo lithography for freely movable 3D micro structure-super IH process with submicron resolution. In: Proceedings of the Eleventh Annual International Workshop on Micro Electro Mechanical Systems: An Investigation of Micro Structures, Sensors, Actuators, Machines and Systems; 1998 Jan 25–29; Heidelberg, Germany. Piscataway: The Institute of Electrical and Electronics Engineers, Inc., 1998. p. 290–5.
[3] Choi JS, Kang HW, Lee IH, Ko TJ, Cho DW. Development of micro-stereolithography technology using a UV lamp and optical fiber. Int J Adv Manuf Tech 2009;41(3–4):281–6.
[4] Shoji S, Smith N, Kawata S. Photofabrication of a photonic crystal using interference of a UV laser. Proc SPIE 1999;3740:541–4.
[5] Neumann J, Wieking KS, Kip D. Direct laser writing of surface reliefs in dry, self-developing photopolymer films. Appl Opt 1999;38(25):5418–21.
[6] Straub M, Ventura M, Gu M. Multiple higher-order stop gaps in infrared polymer photonic crystals. Phys Rev Lett 2003;91(4):043901.
[7] Bertsch A, Zissi S, Jézéquel JY, Corbel S, André JC. Microstereophotolithography using a liquid crystal display as dynamic mask-generator. Microsyst Technol 1997;3(2):42–7.
[8] Vaezi M, Seitz H, Yang S. A review on 3D micro-additive manufacturing technologies. Int J Adv Manuf Tech 2013;67(5–8):1721–54.
[9] Xu G, Zhao W, Tang Y, Lu B. Novel stereolithography system for small size objects. Rapid Prototyping J 2006;12(1):12–7.
[10] Roy NK, Cullinan MA. μ-SLS of metals: Design of the powder spreader, powder bed actuators and optics for the system. In: Proceedings of the 26th Annual International Solid Freeform Fabrication Symposium—An Additive Manufacturing Conference; 2015 Aug 10–12; Austin, TX, USA. Austin: University of Texas at Austin; 2015. p. 134–55.
[11] Awtar S, Parmar G. Design of a large range *XY* nanopositioning system. J Mech Robot 2013;5(2):021008.
[12] Xu Q. Design and development of a compact flexure-based *XY* precision positioning system with centimeter range. IEEE Trans Ind Electron 2014;61(2):893–903.
[13] Zhou X, Wang D, Wang J, Chen SC. Precision design and control of a flexure-based roll-to-roll printing system. Precis Eng 2016;45:332–41.
[14] Kang HW, Jeong YS, Lee SJ, Kim KS, Yun WS. Development of a compact micro-stereolithography (MSTL) system using a Blu-ray optical pickup unit. J Micromech Microeng 2012;22(11):115021.
[15] Hao G, Yu J. Design, modelling and analysis of a completely-decoupled *XY* compliant parallel manipulator. Mech Mach Theory 2016;102:179–95.
[16] Zhang Z, Liu Z, Yan P. Design of a flexure-based XY positioning stage with balanced axial forces on decoupling modules. In: Proceedings of the 6th International Conference on Manipulation, Manufacturing, Measurement on the Nanoscale; 2016 Jul 18–22; Chongqing, China. Piscataway: The Institute of Electrical and Electronics Engineers, Inc.; 2016. p. 83–8.
[17] Yu J, Xie Y, Li Z, Hao G. Design and experimental testing of an improved large-range decoupled *XY* compliant parallel micromanipulator. J Mech Robot 2015;7(4):044503.
[18] Zhang Z, Wang P, Yan P, Guan Y. A beam flexure-based nanopositioning stage supporting laser direct-write nanofabrication. Sci China Phys Mech Astron 2016;59(8):684211.
[19] Awtar S, Slocum AH, Sevincer E. Characteristics of beam-based flexure modules. J Mech Design 2007;129(6):625–39.